# Improving Solar Vapor Generation by Eliminating the Boundary Layer Inhibition Effect of Evaporator Pores

Zhiyang Zhang, Wenlong Xu, Jian Wang,* Mi Hu, Dongming Zhang, Lujie Jia, Azhen Kang, Yonglan Xi, Xiaomei Ye, Shuang Cheng, Enhui Sun, Yu Chen,* Zhijun Wang, Hongzhen Lin,* and Qingbo Xiao*

ABSTRACT: Solar-driven water evaporation is highly demanded in various applications. However, the pore structures of the solar evaporators are commonly randomly designed, which seriously hinder vapor diffusion and thus limit water producibility. Herein, the boundary layer inhibition effect is uncovered for the first time, and we propose that low-tortuosity channels with a reduced boundary layer thickness is adequate for breaking through the long-existing vapor diffusion limitation. As a demo, nature-inspired low-tortuosity channels are constructed for a solar evaporator. Due to elimination of the boundary layer inhibition, the vapor diffusion flux can easily escape from the evaporator, yielding an evaporation rate of 16.8 kg m^{-2} h^{-1} under a convective flow of 4.0 m s^{-1} and 1 sun irradiation. Moreover, the 3D radial interconnection of the channels enables stable water evaporation under an arbitrary direction of convective flow. Our work provides a promising solution to eliminate the boundary layer inhibition effect of a solar evaporator.
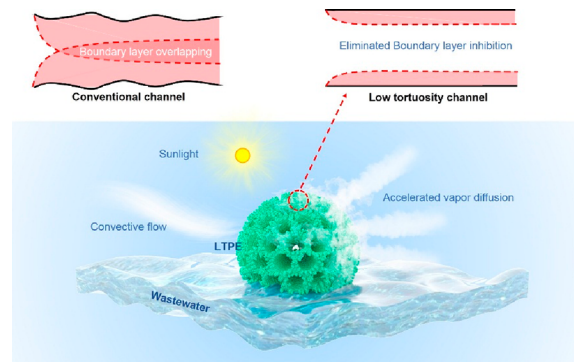
To date, solar-driven interfacial water evaporation has been a hot research topic in view of its various advantages such as energy savings and low cost for water treatment.[1−9] The evaporators based on photothermal materials usually rely on their porous structures to provide a large surface area by closely contacting with water, so as to sufficiently make utilization of the input solar energy. Meanwhile, decorating the photothermal materials with a hydrophilic coating layer or sites could also modulate the states of the adsorbed water, which is further beneficial for efficient water vapor generation.[10] However, in terms of the specific photothermal material, the water vapor diffusion is seriously impeded by the strong stagnation force between the pores and the vapor moisture, which is the crucial rate-determining step that hinders a further increment of the water producibility of the solar evaporators.[11,12]

To address the above challenges, efforts to enhance water vapor diffusion have been devoted to the construction and preparation of various structured porous photothermal materials.[7,11,13−15] However, these pore structures are random and casual without ideal designations. In reality, a flow velocity gradient will be formed along the channel surface due to the presence of the viscous force of the fluid, forming the so-called diffusive boundary layer, which generates a boundary layer

inhibition effect that may seriously hinder vapor diffusion and decrease evaporation efficiency.[16,17] Especially, the boundary layer thickness is significantly enlarged in the random cross-linked pores owing to the strong viscous force induced by factors such as twisted channels and uneven pore size distributions (Figure 1A). According to Carman et al., all these factors can be generalized to a dimensionless parameter, namely hydraulic tortuosity, to reflect the relation between the fluid flow and porous structure.[18−20] The increased tortuosity causes a thick boundary layer in the random pores. Moreover, the boundary layers are more prone to be overlapped in the small-sized channels, which further inhibits vapor diffusion and significantly limits water producibility. According to the extended Darcy's law by Matyka et al.,[20] the relation of vapor flux (q) in a porous matrix and the channel tortuosity (T, $T > 1$) can be generalized as $q \propto 1/T^2$ in the low Reynolds number regime. Because the T
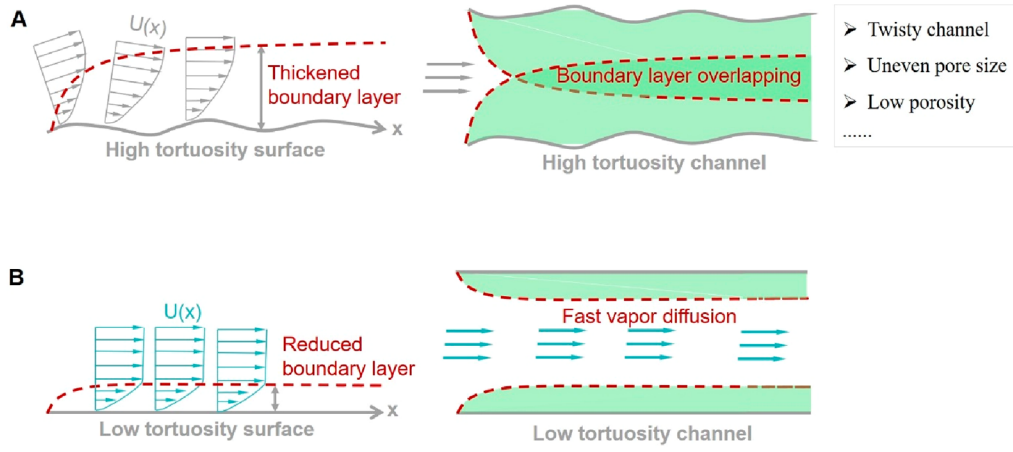
Figure 1. Schematic illustrations of vapor diffusion velocity ($U(x)$) and boundary layer inhibition effect in the (A) high-tortuosity and (B) low-tortuosity channels, respectively.
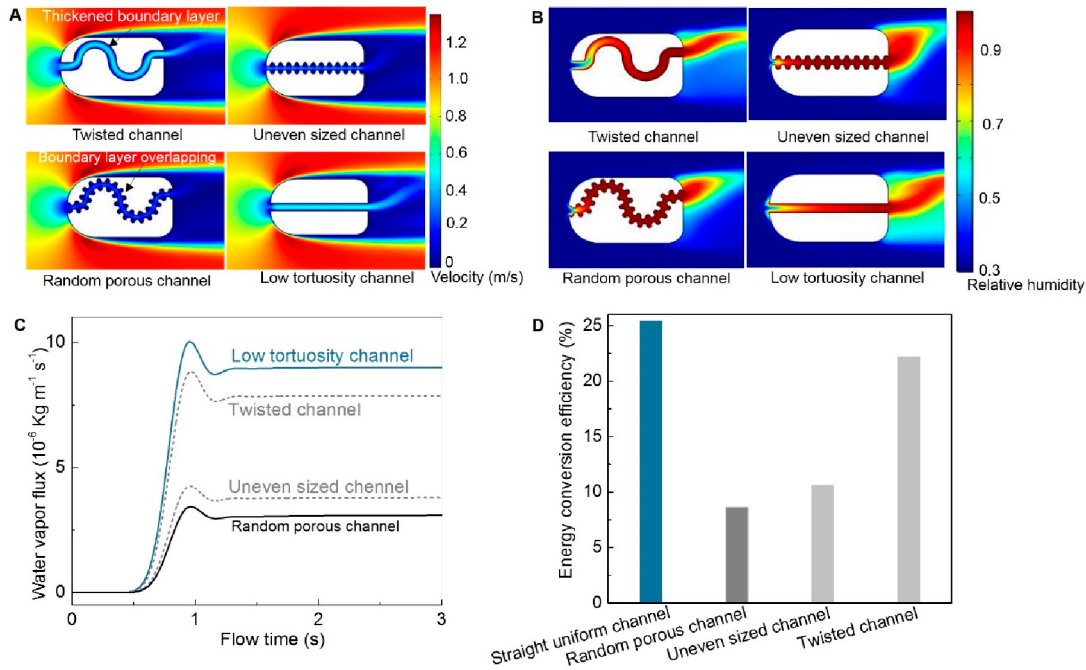

Figure 2. Comparison of boundary layer inhibition effects in different structural channels with an incident convective flow of 1 m s^{-1}. The initial pore diameter and transverse length of the channels are set to be 2 and 24 mm, respectively. (A) Simulation results of vapor diffusion velocities in different channels. (B) Simulation results of relative humidities in different channels. (C) Comparison of the vapor diffusion fluxes in different channels. (D) Calculated wind energy conversion efficiencies in different channels.

value can be increased by 1 or 2 orders of magnitude in the high-tortuosity channels, the vapor diffusion would be overwhelmingly limited in the high-tortuosity random pores. Therefore, eliminating the serious boundary layer inhibition is an effective way and is urgently demanded to further increase the water producibility of solar evaporators. For example, millimeter-scale pores with a large areal surface were fabricated to reduce boundary layer overlapping of a solar evaporator.[11,14] However, despite these efforts, the water evaporation rate of these photothermal materials is still limited to below 12 kg m^{-2} h^{-1}. This can be attributed to the lack of comprehensive understanding of the vapor diffusion kinetics of the solar evaporators, which mainly constructs unoptimized random pore structures with thick boundary layers that still inhibit vapor diffusion. Taking all of this into consideration, providing a clear depiction of vapor diffusion kinetics and ultimately eliminating diffusion

boundary inhibition in the millimeter-scale low-tortuosity channels may be an ideal strategy to realize highly efficient water producibility of solar evaporators (Figure 1B).

Herein, the vapor diffusion kinetics of a solar evaporator is comprehensively determined by a dynamic COMSOL simulation and the boundary layer inhibition effect of the unoptimized random pores is clearly uncovered. Aa a demo, a nature-inspired low-tortuosity porous evaporator (LTPE) is proposed and optimized to break through the long-existing vapor diffusion limitation. In this design, the diffusion boundary layer thickness can be effectively eliminated in the long-distance-ordered low-tortuosity channels, so that the evaporation rate is capable of being enhanced with low diffusion resistance. As a result, the vapor diffusion of the LTPE can be 260% faster than those of conventional evaporators, yielding a record-high water evaporation rate of 16.8 kg m^{-2} h^{-1} under a convective flow rate
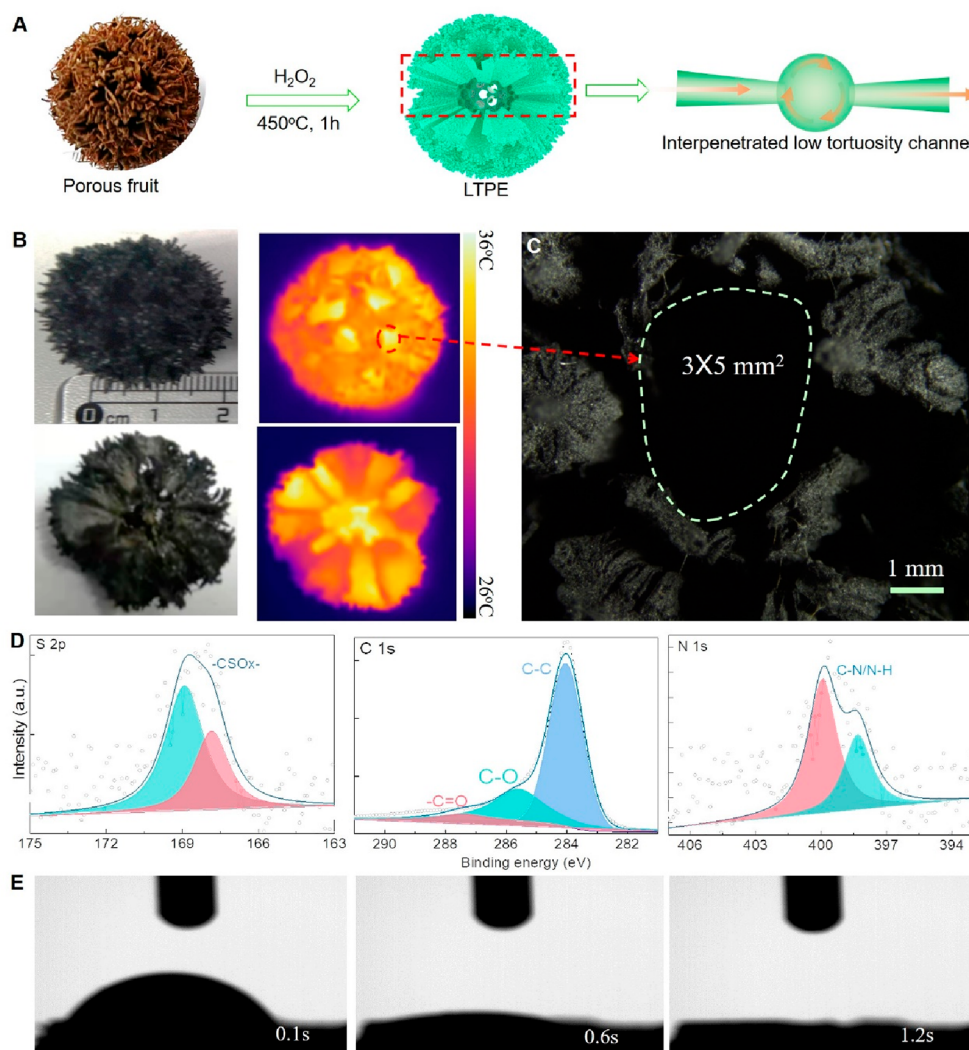
Figure 3. Characterizations of the low-tortuosity channels of the LTPE. (A) Schematic illustrating the preparation procedure and showing the low-tortuosity and 3D-radial-penetrated channels of the LTPE. **(B)** Photographs and infrared images of the whole body and cross section of the LTPE. **(C)** Optical micrograph showing the pore size of the channel. **(D)** XPS spectra of the LTPE, showing the hydrophilic groups C−O, C=O and CSOx, C−N/NH. **(E)** Water contact angle for the LTPE. The water drop rapidly infiltrates in the LTPE within 1.2 s.

of 4.0 m s^{-1} and 1.0 sun irradiation. Moreover, the 3D radial interconnection of the channels also enables stable and fast water evaporation under arbitrary solar irradiation and convective flow for outdoor treatment of wastewater. The easily scalable LTPE sheds light on the feasibility of high-performance and energy-saving solar evaporators by eliminating boundary layer inhibition for fast vapor diffusion kinetics.

To uncover the boundary layer effect on inhibiting the evaporating efficiency, characteristic dynamic simulations on twisted and straight channels of photothermal materials were thoroughly carried out and compared via COMSOL simulations. The numerical simulations were conducted for four types of channels denoted a low-tortuosity channel, twisted channel, uneven-sized channel, and random porous channel, respectively. All of them have the same horizontal length of 24 mm and an average channel diameter of 2 mm (Figure S1). The humidity of the airstream was determined to be 30% RH at a temperature of 25 °C, and the humidity of the channel surface was saturated during the evaporation progress (100% RH). To simulate the boundary layer inhibition effect, other factors such as the inlet and outlet pore diameter as well as the transverse

length were set to be the same for all the channels involved in our simulation (see details in Experimental Procedure S1). As can be clearly observed in Figure 2A, due to the large viscous force generated from the high-tortuosity surface, the boundary layer thickness is enlarged in either the twisted or uneven-sized channels, significantly limiting vapor diffusion therein. Such a condition deteriorates for the random porous channel with an uneven pore size distribution or the twisted channel. The tremendous boundary layer overlap can be observed in the random porous channel, which imposes a huge resistance to vapor diffusion and results in extremely low water vapor velocity. In sharp contrast, the boundary layer thickness is obviously diminished in the low-tortuosity surface due to a much reduced but smooth viscous force, which facilitates fast vapor diffusion. Such distinct vapor diffusion kinetics results in different vapor concentration distributions in the channels. As shown in Figure 2B, in the low-tortuosity channel, fast vapor diffusion is able to entrain a large amount of water vapor out from the channel, leaving a low concentration of the vapor distribution inside the pores. In contrast, the vapor concentration is much higher in the random porous channel. Consistent with the low vapor diffusion
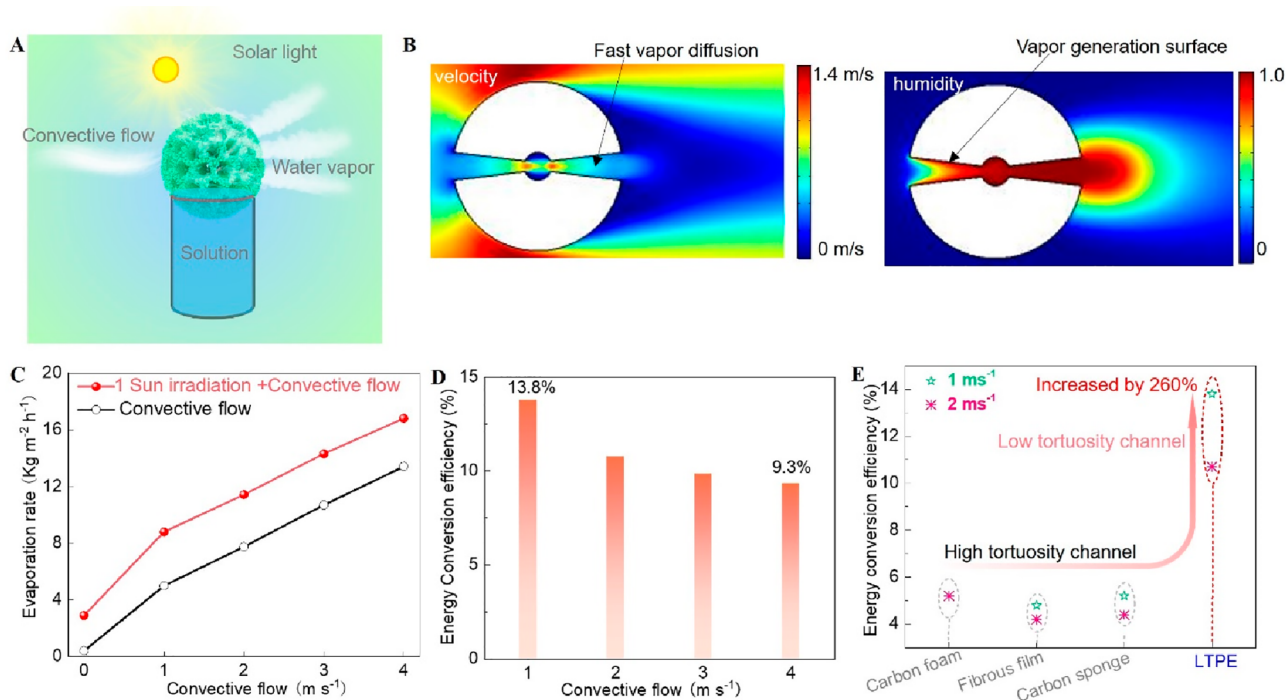
Figure 4. Characterization of the enhanced vapor diffusion via eliminating boundary layer overlap in the low-tortuosity channels. (A) Schematic of the water evaporation of LTPE under combined solar irradiation and convective flow. (B) Simulations of wind velocity and humidity distribution in the channels with an incident flow of 1 m s^{-1}. (C) Evaporation rates of the LTPE under different conditions. (D) Calculated wind-vapor conversion efficiency of the LTPE under different flow velocities. (E) Comparison of the wind-vapor conversion efficiencies of LTPE and previous photothermal materials. The value for carbon foam was obtained from the literature.[11]

velocities in the high-tortuosity channels, most of the water vapor still remains in the random porous channel, as it can hardly diffuse out, causing a dense vapor distribution in the channel. To more precisely uncover the boundary layer inhibition effect, the detailed water vapor fluxes of the channels were also calculated and compared (Figure 2C). By subtracting the vapor flux of the pore inlet from the outlet, the water vapor diffused from different structured channels can be obtained. The amount of water vapor that diffused from the low-tortuosity channel without boundary effects is much higher than that for the high-tortuosity channel. The water vapor flux in the random porous channel accounts for only one-third of that in the low-tortuosity channel, which strongly demonstrates the high effectiveness of eliminating bthe oundary layer thickness to increase the water producibility of solar evaporators. Considering the practical surroundings, the wind-assisted vapor conversion efficiencies (WVCEs) of different channels were also obtained. The conversion efficiency was calculated according to the reported method,[11] $\eta = m_w/m_{con}$, where m_w is the generated water vapor flux from the channels and m_{con} is the theoretical water vapor flux assuming 100% utilization of wind flow, respectively. The detailed calculation method of WVCEs can be found in Experimental Procedure S2. As is compared in Figure 2D, only ~8% of the energy of the convective flow can be utilized by the random porous channel to accelerate vapor diffusion. In sharp contrast, over 25% of the wind energy can be effectively utilized in the ideal low-tortuosity channel, implying a huge improvement in eliminating boundary effects for the pore structure designation strategy to improve the energy utilization efficiency of the water evaporators.

As indicated by the above simulation, the ideal evaporator should possess the superiority of long-distance well-distributed low-tortuosity pores for fast vapor diffusion. Inspired by the natural biomass of *Liquidambar formosana*, a novel LTPE was

obtained via sequential chemical activations to optimize the photothermal performance (Figure 3A). Optical images of the whole body and cross section of the LTPE are shown in Figure 3B,C. The optical images are unable to reflect the detailed structure of the black LTPE; thus, we surveyed the infrared images of the LTPE adsorbing hot water to further display the detailed structures of the low-tortuosity channels of the LTPE. As shown in Figure S2, the low-tortuosity channels are 3D-interpenetrated with an average length of about 24 mm and pore sizes of about 1.5−4.1 mm. Although these are not the "ideal" low-tortuosity channels with a totally even pore size distribution, the surfaces of channels are roughly straight on a centimeter scale, which possess much lower tortuosity as compared to the existing random structured pores. As will be discussed in detail later, such 3D-interpenetrated low-tortuosity channels play a vital role in facilitating fast and stable vapor diffusion. Besides the unique low-tortuosity channels for vapor diffusion, the LTPE also exhibits hierarchal pore structures, as revealed in the scanning electron microscope (SEM) images. The high-resolution SEM images in Figure S3A reveal the presence of a hierarchical porous structure at the LTPE surface. Moreover, the cross section of the LTPE sample exhibits abundant microsized pores of around 5−20 μm (Figure S3B), which are suitable for water evaporation and transportation.[5] The superior hydrophilicity of the LTPE is characterized by X-ray photoelectron spectroscopy (XPS) and a water contact angle test, as well as IR thermal images. The XPS spectra show that the LTPE is mainly composed of C, O and S, N, leading to the formation of the hydrophilic groups C−O, C═O and CSO$_x$, C−N/NH (Figure 3D). The elemental analysis shows that the contents of O, N, and S in the LTPE are 19.75%, 0.48%, and 0.05%, respectively. The water contact angle tests show that the water drop rapidly infiltrates into the sample within 1.2 s, reflecting the high
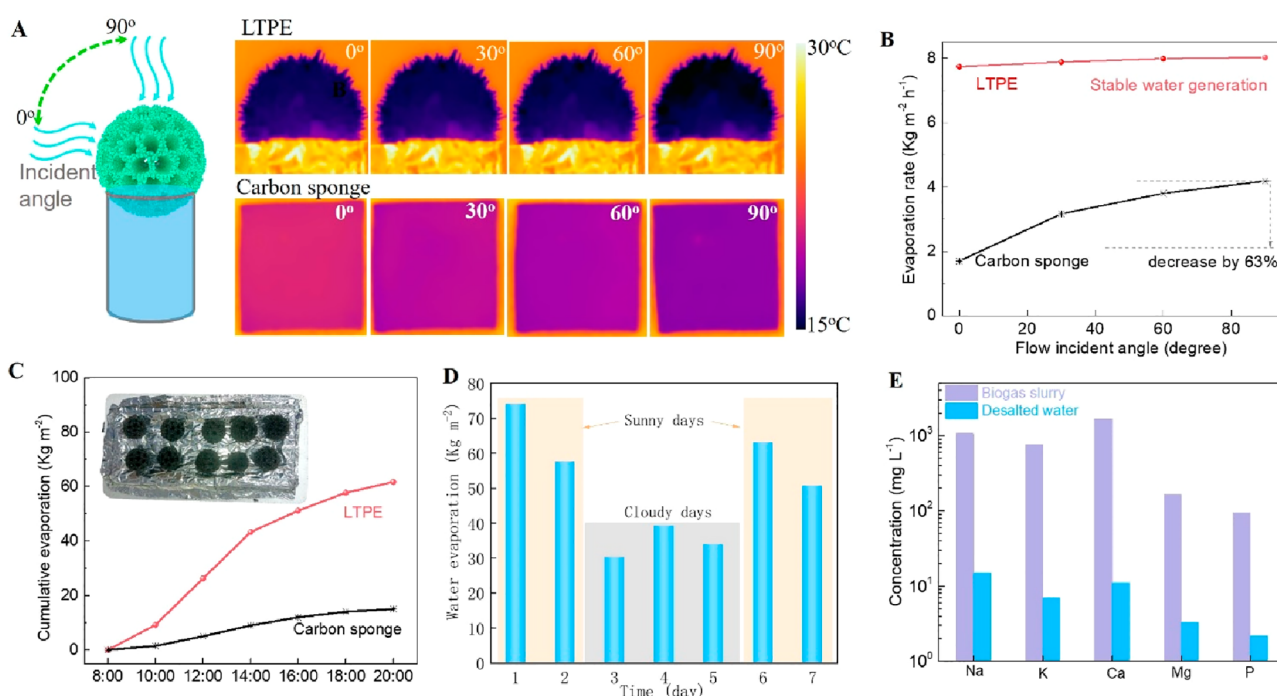
Figure 5. Water evaporation stability of the LTPE for wastewater treatment. (A, B) Comparison of the infrared images and water evaporation rates of the LTPE and a carbon sponge under convective flow from different directions. **(C)** Comparison of the outdoor water evaporation performance of the LTPE with a carbon sponge. The inset illustrates the outdoor large-scale device. **(D)** Long-term test showing the ultrafast outdoor water evaporation performance of the LTPE for treatment of biogas slurry. **(E)** The elements in the recycled water of biogas slurry can be purified to a level meeting the standard of environmentally friendly discharge.

hydrophilicity of the LTPE (Figure 3E). The fast water transportation property of the LTPE is revealed by the IR thermal images (Figure S4). The LTPE has superb solar light absorption and vapor generation properties, which can generate a water evaporation rate of 2.9 kg m^{-2} h^{-1} under merely solar light irradiation of 1 sun (Figure S5), as measured according to a previous method.[21]

The superior vapor diffusion capability of the LTPE was characterized by the combined utilization of wind flow and solar light (Figure 4A) to maximally rule out the boundary layer inhibition. To more clearly demonstrate the vapor diffusion property, the water vapor distribution in the channels of the LTPE was initially simulated. Under a convective flow of 1 m s^{-1}, an extremely thin diffusion boundary layer can be observed for the channel. The flow velocity can be well contained in the channel, which effectively accelerates water vapor diffusing out of the channels (Figure 4B). The low-tortuosity channels with different connect angles were also analyzed (Figure S6), and the simulation results show that the connect angle has no obvious influence on the water vapor flux of the channels. The simulation of multiple channels shows a much higher water vapor flux as compared to a single channel (Figure S7). The above analysis implies that our construction of the low-tortuosity channels in the photothermal evaporator is effective in eliminating boundary layer inhibition.

To imitate a practical surrounding, the vapor diffusion properties of the LTPE were first assessed with convective wind flow. Under a convective flow of 2 m s^{-1} for 5 min, the surface temperature of the TPE decreases from 21 to 15 °C due to largely accelerated water vapor diffusion with the aid of the convective flow (Figure S8). Moreover, thanks to the 3D interpenetration characteristics of the low-tortuosity channels, the convective flow is able to feasibly penetrate to the back side

of the LTPE, and thus vapor diffusion occurs throughout the whole LTPE body. As a result, the temperature of the back surface of the LTPE is also decreased to 16 °C, facilitating the thermal energy collection from the environment.[22] The coupling of convective flow (2 m s^{-1}) with 1 sun irradiation increases the LTPE temperature results to a surface temperature of ~25 °C (Figure S9), which is much lower than that of solely 1 sun irradiation (33 °C). To further test the vapor diffusion capability of the low-tortuosity channels, the water evaporation rates of the LTPE were measured under a combined convective flow and 1 sun irradiation. As summarized in Figure 4C, the LTPE yields fast water evaporation rates of 8.8, 11.4, 14.3, and 16.8 kg m^{-2} h^{-1}, respectively, when coupling the 1 sun irradiation with a convective flow ranging from 1 to 4 m s^{-1}. To further uncover the roles of the low-tortuosity channels in vapor diffusion, these millimeter-sized pores were filled with common porous carbon and their water evaporation capabilities were thoroughly compared, as shown in Figure S10. The Brunauer−Emmett−Teller (BET) measurements show that the surface area of the LTPE changes from 908 to 891 m^2/g after filling with common carbon. Consistent with the surface area measurements, the water evaporation rate of the samples remains nearly stable under 1 sun irradiation. However, under a convective flow of 2 m s^{-1}, the water evaporation rate of the LTPE decreases from 7.7 to 3.7 kg m^{-2} h^{-1} after filling with common carbon. Even under combined 1 sun irradiation and convective flow, the evaporation rate of the common carbon filled LTPE is only 6.5 kg m^{-2} h^{-1}, much lower than the 11.4 kg m^{-2} h^{-1} of the sample exhibiting low-tortuosity channels. Obviously, without the low-tortuosity channels, only the vapor generated at the external surface of the LTPE can be readily diffused, and the vapor diffusion in the inner part of the sample is largely inhibited, causing slow water evaporation even under a convective flow. Undoubtedly, the

low-tortuosity channels play a critical role in eliminating the boundary layer inhibition effect.

The fast vapor diffusion capability of the LTPE is further reflected by calculating its wind-vapor convention efficiency (Experimental Procedure S2). As can be seen in Figure 4D, the WVCE of the LTPE reaches as high as 13.8% at a weak convective flow of 1 m s^{-1}. Even at a wind velocity of 4 m s^{-1}, the WVCE of the LTPE is still greater than 9%. For comparison, the evaporation performances of two conventional high-tortuosity porosity photothermal materials were also measured (Figures S11 and S12).[23,24] The WVCEs of these photothermal materials were calculated and are compared in Figure 4E. It can be seen that the LTPE sample exhibits the largest efficiency of wind-vapor conversion, which is ∼260% times those of other photothermal materials ever reported previously. Given that the vapor generation capabilities are the same for all these solar-water evaporation systems, it is can be deduced that the vapor diffusion speed in the low-tortuosity channels of LTPE is ∼260% times faster than that of other evaporators under the same condition. Thanks to the low-tortuosity channels enhancing vapor diffusion, the LTPE yields a record-high evaporation rate of 16.8 kg m^{-2} h^{-1} under 1 sun irradiation and a convective flow of 4 m s^{-1}, which is overwhelmingly larger than the previously reported 11.9 and 10.9 kg m^{-2} h^{-1} obtained under the same evaporation conditions.[11,25] In view of the inherent temporal and spatial complementarity of wind flow and solar light, the coupling of these two green energies in one evaporator is of vital importance for expanding the usage scenario of the solar water evaporation technique.

Keeping stable vapor diffusion under arbitrary directions of natural wind flow and solar irradiation is highly important for the outdoor application of a solar evaporator. The 3D-interpenetrated character of the low-tortuosity channels enables stable water producibility of the LTPE due to its boundary layer thickness being independent of the incident convective flow. The dependence of water evaporation on the incident angles of convective flow is tested for the LTPE (Figure 5A). There is almost no obvious change of the surface temperature for LTPE with the variation of incident angles as detected by IR thermal images. In contrast, the surface temperature of a conventional carbon sponge is highly vulnerable to the wind flow direction. With the wind flow direction varying from 0 to 90° at a velocity of 2 m s^{-1}, the water evaporation rate only changes slightly from 7.7 to 8.0 kg m^{-2} h^{-1}, but the water evaporation rate of the carbon sponge shape decreases from 3.2 to 1.3 kg m^{-2} h^{-1} (Figure 5B). These results reflect that the 3D interpenetrated pores of the LTPE guarantees a stable vapor diffusion capability under arbitrary directions of wind flow. The outdoor water evaporation stability of the LTPE was demonstrated using a prototype device (Figure 5C and Figure S13). The outdoor conditions including incident sunlight flux, natural convective flow, and ambient temperature are recorded in Figure S14. After a continuous 12 h exposure to the coupled natureal wind and solar light, the LTPE yields a cumulative mass change of 47 kg m^{-2} and an average water evaporation rate of 3.9 kg m^{-2} h^{-1}, which is much higher than that of a carbon sponge evaporator (1.2 kg m^{-2} h^{-1}). Using the indoor evaporation rate under a wind flow incident angle of 90° as a reference, it can be seen that the LTPE exhibits superior outdoor evaporation stability compared to the carbon sponge (Table S1). In addition to the convective flow direction, we also measured the water evaporation of the LTPE in salt solution, since the salt crystal accumulation at the surface may also block the convective flow.

As can be seen in Figure S15, the salt has nearly no influence on the water evaporation of the LTPE when under 1 sun irradiation, and the evaporation rates only decrease by ∼16% after a continuous operation of 8 h under a combined 1 sun irradiation and convective flow of 4 m s^{-1}. Moreover, the evaporation rates can be feasibly recovered merely by stopping the convective flow to let the salt crystals dissolve. The salt resistance of the LTPE may be due to its hierarchal millimeter- and micrometer-sized pores, which provide sufficient channels to back-transfer the concentrated salt solution to water.

To further prove the great potential of the as-prepared LTPE sample for practical water evaporation applications, outdoor wastewater remediation with zero liquid discharge was performed using a biogas slurry as a proof-of-concept demonstration. As a typical wastewater pollutant in agriculture, a biogas slurry is rich with active nutrients such as phosphorus (P) and potassium (K), which are highly demanded for crop production. To reduce the transportation cost from the livestock to farmland, it is recommended that the biogas slurry can be concentrated and used as an intensive liquid fertilizer by getting rid of the high content of water.[26,27] However, the existing methods for concentrating biogas slurry such as vacuum evaporation and membrane technology have either a high energy consumption or a high cost. We demonstrate that the biogas slurry can be readily concentrated by using the LTPE to drive fast water evaporation in a natural environment. As can be seen in Figure 5D, the water evaporation rate of LTPE toward the biogas slurry reaches 50−76 kg m^{-2} d^{-1} on sunny days and 30−39 kg m^{-2} d^{-1} on cloudy days, generating an average outdoor evaporation rate of ∼51 kg m^{-2} d^{-1}. Assuming the production of biogas slurry in a scaled livestock farm is 20 t d^{-1}, it can be estimated that only ∼400 m^2 of the as-prepared LTPE sample is needed for treating this wastewater. The release of some primary elements (Na, K, Ca, Mg, and P) from the biogas slurry is tested by measuring their concentrations in the recovered water, which are all reduced by over 2 orders and are below the corresponding required concentrations for effluent discharge (Figure 5E).[28] Thus, the evaporated water by the LTPE can be directly discharged in the environment and the concentrated biogas slurry could be recovered as an intensive liquid fertilizer. Considering its high solar and wind energy utilization efficiency, the as-prepared LTPE is very promising to be used for energy-saving wastewater treatment.

In summary, the vapor diffusion kinetics in the solar evaporators is comprehensively understood for the first time by a dynamic COMSOL simulation. These results demonstrate that the boundary layer inhibition effect of the unoptimized random pores seriously limits the water evaporation efficiency of current evaporators. The simulations also show that the boundary layer thickness can be largely reduced in the low-tortuosity channels, which play decisive roles in breaking through the long-existing vapor diffusion limitation. As a demo, a nature-inspired low-tortuosity photothermal evaporator was prepared and optimized via sequential chemical activations, which yields a record-high water evaporation rate of 16.8 kg m^{-2} h^{-1} under convective flow rate of 4.0 m s^{-1} and 1 sun irradiation. Due to effectively eliminated boundary layer inhibition, the vapor diffusion flux of the LTPE is about 260% greater than those of other evaporators ever reported before. Moreover, benefiting from the 3D-interpenetrated character of the low-tortuosity channels, the LTPE retains stable water evaporation under arbitrary directions of solar light and wind flow. An outdoor experiment yields a large water evaporation rate of 51 kg

$m^{-2} d^{-1}$ using biogas slurry as a proof-of-concept demonstration, suggesting its potential for a fast and energy-saving wastewater treatment. Our work brings new insight into understanding the vapor diffusion kinetics of a solar evaporator. The proposed low-tortuosity channels should open new avenues for eliminating the diffusion boundary layer inhibition and thus increasing the water producibility of the solar evaporation technique.

AUTHOR INFORMATION

Corresponding Authors

Jian Wang − *i-Lab, Suzhou Institute of Nano-tech and Nano-bionics, Chinese Academy of Sciences, Suzhou 215123, People's Republic of China; Helmholtz Institute Ulm (HIU), Ulm D89081, Germany;* orcid.org/0000-0002-7945-0826; Email: jian.wang@kit.edu, wangjian2014@sinano.ac.cn

Yu Chen − *Institute of Advanced Materials, Chengdu University, Chengdu 610106, People's Republic of China;* Email: chenyu01@cdu.edu.cn

Hongzhen Lin − *i-Lab, Suzhou Institute of Nano-tech and Nano-bionics, Chinese Academy of Sciences, Suzhou 215123, People's Republic of China;* Email: hzlin2010@sinano.ac.cn

Qingbo Xiao − *Institute of Agricultural Resources and Environment, Jiangsu Academy of Agricultural Sciences, Nanjing 210014, People's Republic of China; Key Laboratory of Agro-Environment in Downstream of Yangtze Plain, Ministry of Agriculture and Rural Affairs, Nanjing 210014, People's Republic of China;* orcid.org/0000-0002-1758-8512; Email: qbxiao@jaas.ac.cn

Authors

Zhiyang Zhang − *Institute of Agricultural Resources and Environment, Jiangsu Academy of Agricultural Sciences, Nanjing 210014, People's Republic of China; Key Laboratory of Agro-Environment in Downstream of Yangtze Plain, Ministry of Agriculture and Rural Affairs, Nanjing 210014, People's Republic of China;* orcid.org/0000-0001-5843-4096

Wenlong Xu − *Institute of Agricultural Resources and Environment, Jiangsu Academy of Agricultural Sciences, Nanjing 210014, People's Republic of China; Key Laboratory of Agro-Environment in Downstream of Yangtze Plain, Ministry of Agriculture and Rural Affairs, Nanjing 210014,*

People's Republic of China; orcid.org/0000-0002-0091-4238

Mi Hu − *Institute of Agricultural Resources and Environment, Jiangsu Academy of Agricultural Sciences, Nanjing 210014, People's Republic of China; Key Laboratory of Agro-Environment in Downstream of Yangtze Plain, Ministry of Agriculture and Rural Affairs, Nanjing 210014, People's Republic of China*

Dongming Zhang − *Institute of Advanced Materials, Chengdu University, Chengdu 610106, People's Republic of China*

Lujie Jia − *i-Lab, Suzhou Institute of Nano-tech and Nano-bionics, Chinese Academy of Sciences, Suzhou 215123, People's Republic of China*

Azhen Kang − *Department of Bridge Engineering, School of Civil Engineering, Southwest Jiaotong University, Chengdu 610031, People's Republic of China*

Yonglan Xi − *Institute of Agricultural Resources and Environment, Jiangsu Academy of Agricultural Sciences, Nanjing 210014, People's Republic of China*

Xiaomei Ye − *Institute of Agricultural Resources and Environment, Jiangsu Academy of Agricultural Sciences, Nanjing 210014, People's Republic of China*

Shuang Cheng − *i-Lab, Suzhou Institute of Nano-tech and Nano-bionics, Chinese Academy of Sciences, Suzhou 215123, People's Republic of China*

Enhui Sun − *Institute of Agricultural Resources and Environment, Jiangsu Academy of Agricultural Sciences, Nanjing 210014, People's Republic of China*

Zhijun Wang − *Institute of Advanced Materials, Chengdu University, Chengdu 610106, People's Republic of China*

Author Contributions

Z.Z. and W.X. contributed equally to this work. Z.Z. and W.X. performed the experiments and analyzed the data. D.Z., Y.C., A.K. and Z.W. performed the simulation. M.H. performed the experiments. J.W. analyzed the data and wrote the manuscript. S.C., X.Y., Y.X., L.J. and E.S. provided helpful discussions. H.L. conceived the idea and analyzed the data. Q.X. conceived the idea, analyzed the data, and wrote the manuscript.

Notes

The authors declare no competing financial interest.

REFERENCES

(1) Zhang, P. P.; Zhao, F.; Shi, W.; Lu, H. Y.; Zhou, X. Y.; Guo, Y. H.; Yu, G. H. Super Water-Extracting Gels for Solar-Powered Volatile Organic Compounds Management in the Hydrological Cycle. *Adv. Mater.* **2022**, *34*, 2110548.

(2) Guo, Y. H.; de Vasconcelos, L. S.; Manohar, N.; Geng, J. F.; Johnston, K. P.; Yu, G. H. Highly Elastic Interconnected Porous Hydrogels through Self-Assembled Templating for Solar Water Purification. *Angew. Chem., Int. Ed.* **2021**, *61*, e202114074.

(3) Zhang, Y. X.; Zhang, H.; Xiong, T.; Qu, H.; Koh, J. J.; Nandakumar, D. K.; Wang, J.; Tan, S. C. Manipulating unidirectional fluid transportation to drive sustainable solar water extraction and brine-drenching induced energy generation. *Energy Environ. Sci.* **2020**, *13* (12), 4891−4902.

(4) Ding, T. P.; Zhou, Y.; Ong, W. L.; Ho, G. W. Hybrid solar-driven interfacial evaporation systems: Beyond water production towards high solar energy utilization. *Mater. Today* **2021**, *42*, 178−191.

(5) Chen, X.; He, S. M.; Falinski, M. M.; Wang, Y. X.; Li, T.; Zheng, S. X.; Sun, D. Y.; Dai, J. Q.; Bian, Y. H.; Zhu, X. B.; Jiang, J. Y.; Hu, L. B.; Ren, Z. J. Sustainable off-grid desalination of hypersaline waters using Janus wood evaporators. *Energy Environ. Sci.* **2021**, *14* (10), 5347−5357.

(6) Zheng, S. X.; Yang, M. Q.; Chen, X.; White, C. E.; Hu, L. B.; Ren, Z. J. Upscaling 3D Engineered Trees for Off-Grid Desalination. *Environ. Sci. Technol.* **2022**, *56* (2), 1289−1299.

(7) Wang, Y. D.; Wu, X.; Gao, T.; Lu, Y.; Yang, X. F.; Chen, G. Y.; Owens, G.; Xu, H. L. Same materials, bigger output: A reversibly transformable 2D-3D photothermal evaporator for highly efficient solar steam generation. *Nano Energy* **2021**, *79*, 105477.

(8) Guo, Y. H.; Lu, H. Y.; Zhao, F.; Zhou, X. Y.; Shi, W.; Yu, G. H. Biomass-Derived Hybrid Hydrogel Evaporators for Cost-Effective Solar Water Purification. *Adv. Mater.* **2020**, *32* (11), 1907061.

(9) Gao, T.; Wu, X.; Wang, Y.; Owens, G.; Xu, H. A Hollow and Compressible 3D Photothermal Evaporator for Highly Efficient Solar Steam Generation without Energy Loss. *Sol. RRL* **2021**, *5* (5), 2100053.

(10) Zhou, X. Y.; Guo, Y. H.; Zhao, F.; Yu, G. H. Hydrogels as an Emerging Material Platform for Solar Water Purification. *Acc. Chem. Res.* **2019**, *52* (11), 3244−3253.

(11) Li, J. L.; Wang, X. Y.; Lin, Z. H.; Xu, N.; Li, X. Q.; Liang, J.; Zhao, W.; Lin, R. X.; Zhu, B.; Liu, G. L.; Zhou, L.; Zhu, S. N.; Zhu, J. Over 10 kg m^{-2} h^{-1} Evaporation Rate Enabled by a 3D Interconnected Porous Carbon Foam. *Joule* **2020**, *4* (4), 928−937.

(12) Gao, T.; Wang, Y.; Wu, X.; Wu, P.; Yang, X.; Li, Q.; Zhang, Z.; Zhang, D.; Owens, G.; Xu, H. More from less: improving solar steam generation by selectively removing a portion of evaporation surface. *Sci. Bull.* **2022**, *67* (15), 1572−1580.

(13) Han, D. D.; Chen, Z. D.; Li, J. C.; Mao, J. W.; Jiao, Z. Z.; Wang, W.; Zhang, W.; Zhang, Y. L.; Sun, H. B. Airflow Enhanced Solar Evaporation Based on Janus Graphene Membranes with Stable Interfacial Floatability. *Acs Appl. Mater. Inter.* **2020**, *12* (22), 25435−25443.

(14) Liu, X. H.; Liu, Z. C.; Mishra, D. D.; Chen, Z. H.; Zhao, J.; Hu, C. Q. Evaporation rate far beyond the input solar energy limit enabled by introducing convective flow. *Chem. Eng. J.* **2022**, *429*, 132335.

(15) Lu, H. Y.; Shi, W.; Zhao, F.; Zhang, W. J.; Zhang, P. X.; Zhao, C. Y.; Yu, G. H. High-Yield and Low-Cost Solar Water Purification via Hydrogel-Based Membrane Distillation. *Adv. Funct. Mater.* **2021**, *31* (19), 2101036.

(16) Na, B. C.; Webb, R. L. Mass transfer on and within a frost layer. *Int. J. Heat. Mass. Trans.* **2004**, *47* (5), 899−911.

(17) Wu, J. S.; Yu, B. M.; Yun, M. J. A resistance model for flow through porous media. *Transport Porous Med.* **2008**, *71* (3), 331−343.

(18) Matyka, M.; Khalili, A.; Koza, Z. Tortuosity-porosity relation in porous media flow. *Phys. Rev. E* **2008**, *78* (2), 026306.

(19) Carman, P. C. Fluid flow through granular beds. *Chem. Eng. Res. Des.* **1997**, *75*, S32−S48.

(20) Koponen, A.; Kataja, M.; Timonen, J. Tortuous flow in porous media. *Phys. Rev. E* **1996**, *54* (1), 406−410.

(21) Li, X.; Ni, G.; Cooper, T.; Xu, N.; Li, J.; Zhou, L.; Hu, X.; Zhu, B.; Yao, P.; Zhu, J. Measuring Conversion Efficiency of Solar Vapor Generation. *Joule* **2019**, *3* (8), 1798−1803.

(22) Li, X. Q.; Li, J. L.; Lu, J. Y.; Xu, N.; Chen, C. L.; Min, X. Z.; Zhu, B.; Li, H. X.; Zhou, L.; Zhu, S. N.; Zhang, T. J.; Zhu, J. Enhancement of Interfacial Solar Vapor Generation by Environmental Energy. *Joule* **2018**, *2* (7), 1331−1338.

(23) Gong, F.; Li, H.; Wang, W. B.; Huang, J. G.; Xia, D. W.; Liao, J. X.; Wu, M. Q.; Papavassiliou, D. V. Scalable, eco-friendly and ultrafast solar steam generators based on one-step melamine-derived carbon sponges toward water purification. *Nano Energy* **2019**, *58*, 322−330.

(24) Zhu, B.; Kou, H.; Liu, Z. X.; Wang, Z. J.; Macharia, D. K.; Zhu, M. F.; Wu, B. H.; Liu, X. G.; Chen, Z. G. Flexible and Washable CNT-Embedded PAN Nonwoven Fabrics for Solar-Enabled Evaporation and Desalination of Seawater. *Acs Appl. Mater. Inter.* **2019**, *11* (38), 35005−35014.

(25) Chen, Y. Q.; Wang, Y. D.; Xu, J.; Ibn Raihan, M. R.; Guo, B.; Yang, G.; Li, M. Y.; Bao, H. F.; Xu, H. L. A 3D Opened Hollow Photothermal Evaporator for Highly Efficient Solar Steam Generation. *Sol. RRL* **2022**, *6*, 2200202.

(26) Bonmati, A.; Flotats, X. Pig slurry concentration by vacuum evaporation: Influence of previous mesophilic anaerobic digestion process. *J. Air Waste Manage* **2003**, *53* (1), 21−31.

(27) Zheng, T. X.; Qiu, Z. L.; Dai, Q. Z.; Chen, J. M. Study of biogas slurry concentrated by reverse osmosis system: characteristics, optimization, and mechanism. *Water Environ. Res.* **2019**, *91* (11), 1447−1454.

(28) Ministry of Ecology and Environment of the People's Republic of China. Discharge standard of pollutants for livestock and poultry breeding, accessed 1 January 2003, http://www.gov.cn/fuwu/bzxxcx/bzh.htm.